Research Article

Najmeh Abbasirad*, Angela Barreda, Dennis Arslan, Michael Steinert, Stefan Fasold, Carsten Rockstuhl, Isabelle Staude, Frank Setzpfandt and Thomas Pertsch

Investigation of dipole emission near a dielectric metasurface using a dual-tip scanning near-field optical microscope

https://doi.org/10.1515/nanoph-2021-0429
Received August 5, 2021; accepted October 12, 2021;
published online October 22, 2021

Abstract: A wide variety of near-field optical phenomena are described by the interaction of dipole radiation with a nanophotonic system. The electromagnetic field due to the dipole excitation is associated with the Green's function. It is of great interest to investigate the dipole interaction with a photonic system and measure the near-field Green's function and the quantities it describes, e.g., the local and cross density of optical states. However, measuring the near-field Green's function requires a point-source excitation and simultaneous near-field detection below the diffraction limit. Conventional single-tip near-field optical microscope (SNOM) provides either a point source excitation or amplitude and phase detection with subwavelength spatial resolution. The automated dual-tip SNOM, composed of two tips, has overcome the experimental challenges for simultaneous near-field excitation and detection. Here, we investigate the dipole emission in the near-field of a dielectric metasurface using the automated dual-tip SNOM. We have analyzed the near-field pattern and directional mode propagation depending on the position of the dipole emission relative to the metasurface. This study is one further step toward measuring the dyadic Green's function and related quantities such as cross density of optical states in complex nanophotonic systems for both visible and near-infrared spectra.

Keywords: dielectric metasurface; dipole emission; dual-tip SNOM; Green's function; near-field; partial LDOS.

***Corresponding author**: **Najmeh Abbasirad**, Institute of Applied Physics, Abbe Center of Photonics, Friedrich Schiller University Jena, Albert Einstein Str. 15, 07745 Jena, Germany,
E-mail: najmeh.abbasirad@uni-jena.de. https://orcid.org/0000-0001-9289-6016
Angela Barreda, **Dennis Arslan and Isabelle Staude**, Institute of Applied Physics, Abbe Center of Photonics, Friedrich Schiller University Jena, Albert Einstein Str. 15, 07745 Jena, Germany; and Institute of Solid State Physics, Friedrich Schiller University Jena, Max-Wien-Platz 1, 07743 Jena, Germany
Michael Steinert, **Stefan Fasold and Frank Setzpfandt**, Institute of Applied Physics, Abbe Center of Photonics, Friedrich Schiller University Jena, Albert Einstein Str. 15, 07745 Jena, Germany
Carsten Rockstuhl, Institute of Theoretical Solid State Physics, Karlsruhe Institute of Technology, Wolfgan-Gaede-Str. 1, 76131 Karlsruhe, Germany; and Institute of Nanotechnology, Karlsruhe Institute of Technology, PO-Box 3640, 76021 Karlsruhe, Germany
Thomas Pertsch, Institute of Applied Physics, Abbe Center of Photonics, Friedrich Schiller University Jena, Albert Einstein Str. 15, 07745 Jena, Germany; and Fraunhofer Institute for Applied Optics and Precision Engineering, Albert Einstein Str. 7, 07745 Jena, Germany

1 Introduction

Designing photonic nanostructures to manipulate electromagnetic field distribution allows more precise control of the light–matter interaction on a fundamental level. As one of the most promising examples, the emission and absorption of light by quantum emitters depends sensitively on the nano-environment into which the quantum emitters are integrated. Consequently, integrating quantum emitters into photonic systems enables novel single-photon technologies for quantum information processing [1, 2] and quantum sensing [3–5]. Different designs for suitably nanostructured environments, either made from plasmonic [6, 7] or dielectric [8, 9] photonic materials, were considered to control the emission of the quantum emitters. The quantity describing the quantum emitter's interaction with photonic systems is the local density of optical states (LDOS). It quantifies the number of modes the emitter couples into at a particular spatial position and emission frequency. According to its definition, the LDOS is related to the imaginary part of the dyadic Green's function [10]. Here, the Green's function expresses the field in a given system in response to an electric or magnetic

dipolar point source. Thus, the Green's function can be the basis to explain a wide range of optical phenomena. We stress that the Green's function can also be defined for higher-order multipolar emitters. Nevertheless, the electric and magnetic dipoles remain most central thanks to the correspondence to suitable emitters. Scanning near-field optical microscopy was one of the first techniques proposed to measure the LDOS of nanostructured optical systems using the dipole emission of the SNOM's probe. When operated in the illumination mode, the light emanating from the SNOM's probe mimics the dipole radiation. It was shown theoretically and experimentally that the detected signal in the far-field using the illumination SNOM is related to the partial LDOS [11, 12]. The excitation and detection through one probe in the illumination/collection SNOM configuration with just a single tip were also used to measure the near-field spectra of quantum emitters embedded in photonic crystal cavities [13, 14]. Recently, illumination/collection SNOM measured the imaginary and real part of the electric and magnetic mode volume from selected photonic crystal nanocavities [15, 16]. Likewise, SNOM has mapped Anderson localization, and the speckle pattern in the near-field of disordered photonic crystals where light interference leads to random mode confinement with a small spatial extent [17–20]. However, the single-tip illumination/collection SNOM cannot map the near-field pattern around the excitation point and the extent of the near-field distribution. In complex structured media, the complicated spatial near-field distribution is described by the spatial correlation function [21]. The imaginary part of the dyadic Green's function is also responsible for the spatial correlation function in the near-field region of a random medium [22]. Moreover, the cross density of states (CDOS) that accounts for the spatial coherence between the point source dipole and the point of interest in a disordered photonic system is related to the imaginary part of the Green's function [23–25]. All the quantities mentioned above are associated with the dyadic Green's function of a photonic system [26]. Hence, measuring the dyadic Green's function as the system response function provides deeper insights into the underlying physics of optical phenomena in complex photonic systems. These measurements require a technique with a simultaneous dipole excitation and detecting the amplitude and phase of the electromagnetic near-field components with a high spatial resolution. While microwave measurements of the Green's function have been recently reported [27], the measurement for a visible and near-infrared spectrum has not been addressed yet due to experimental challenges. Regardless of the experimental challenges, the automated dual-tip SNOM is potentially the only instrument that opens avenues toward measuring the near-field dyadic Green's function for the visible and near-infrared spectra [28]. The dual-tip SNOM is composed of two aperture tips, which simultaneously excite and detect electromagnetic fields within the near-field region. In perspective, the integration of phase-sensitive measurement into the dual-tip SNOM would even enable the full vectorial measurement of all electromagnetic field components [29, 30].

Thus far, the dual-tip SNOM was merely used to map the near-field distribution of the plasmonic modes on flat and unstructured metallic surfaces [31–34]. Attempts toward bringing two tips as close as possible to each other led to the realization of a fully automated dual-tip SNOM, capable of collecting optical signals even closer to the excitation point [28]. Nevertheless, the capability of the automated dual-tip SNOM to map out near-fields of structured materials has remained elusive until now.

In this work, the automated dual-tip SNOM has been used to investigate, as a proof of principle, the position-dependent near-field intensity distribution and directional mode propagation upon dipole emission near a nanostructured sample. For this purpose, we used a silicon all-dielectric metasurface since it is a promising platform to realize complex photonic systems [35, 36]. The coupling strength of the illumination into the metasurface varies with the position of the point source excitation relative to the metasurface [37]. Despite the weak light scattering caused by silicon nanodisks at the resonance wavelength, dual-tip SNOM allowed mapping the distinct near-field intensity patterns. Finally, we have verified that the integrated mapped near-field using the dual-tip SNOM can be related to the partial LDOS. This work is also one step further toward mapping the dyadic Green's function and the CDOS for the complex nanophotonic systems.

2 Experimental setup

Our experimental setup consists of two SNOM scanning heads (MV-4000, Nanonics Imaging Ltd) with two aperture tips for excitation and detection below the diffraction limit. In the experiment, the excitation tip illuminated a dielectric metasurface with the dipole-like emission, and the detection tip simultaneously scanned the near-field of the metasurface, mapping optical near-field information around the excitation tip (Figure 1A). The aperture tips in the dual-tip SNOM setup are tapered optical fibers with 200–300 nm Cr–Au coating. The fiber tips make an angle of 30° with the surface normal. The excitation tip, a single-mode fiber, is connected to a tunable laser source

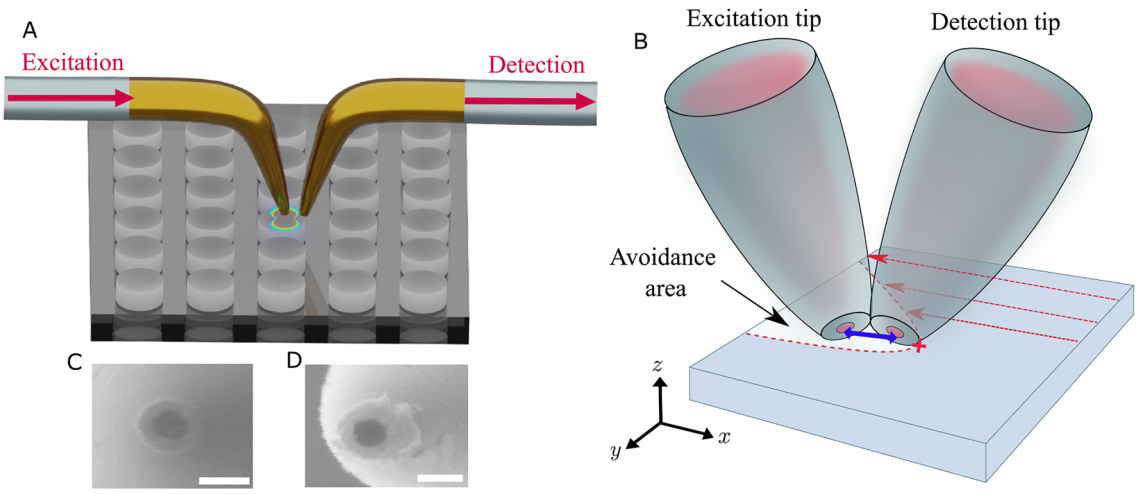

Figure 1: (A) Dual-tip SNOM configuration on top of a silicon nanodisk metasurface. (B) Two aperture tips when they are positioned at the minimum distance from each other. The red dashed arrows show the direction of the scan. The length of the double-sided blue arrow indicates the minimum distance between the apertures. The parabolic white area is the avoidance area (the red dashed curve corresponds to its boundary). The red cross denotes the vertex of the avoidance area. Scanning electron micrograph of the aperture of the (C) excitation tip and (D) detection tip. Scale bars are 0.5 µm.

(Tunics Reference, Anritsu), whereas a multi-mode fiber tip as a detection tip is connected to a single-photon detector (id220, ID Quantique). The aperture diameters of the excitation and detection tips are about 350 nm (Figure 1C and D). In the dual-tip SNOM configuration used for near-field measurements, the excitation tip is stationary and placed at the position of interest on the top of the metasurface inside a scan window, e.g., a square area where the detection tip performs scanning around the excitation tip. A fully digital scanning probe microscope controller (R9, RHK Technology) governs the tip-sample distance during the scan and enables an automated collision prevention scheme to prevent the collision between the two tips when they are laterally close.

In the measurements by dual-tip SNOM setup, the detection tip starts scanning toward the excitation tip (Figure 1B) along the negative x-direction from the corner of the scan window. Optical and topography data are mapped simultaneously (Figure S1, Supplementary Information). The detection tip is controlled in such a way that it does not collide with the excitation tip [28]. Since the geometry of the tips' apex is almost conical, a parabolic-like region called the avoidance area is created during the scan. The parabolic red dashed curve in Figure 1B indicates the boundary of the avoidance area. The geometries of the excitation and detection tips define the boundary of the avoidance area, where the detection tip cannot scan further and sweeps back to the beginning of the next scan line.

A minimum distance between the excitation and detection tip can only be determined when the detection tip scans along the line, which crosses the vertex of the avoidance area (red cross in Figure 1B). The minimum distance corresponds to the distance from the center of the detection tip to the center of the excitation tip. Therefore, the scanning electron microscope (SEM) images of the excitation and detection tips are required before the experiment in order to calculate the minimum distance. The SEM images of the excitation and detection tips are shown in Figure 1C and D, respectively. In these measurements, the minimum distance (Figure 1B, double-sided blue arrow) is about 650 nm between the excitation and detection tip (center to center).

One additional parameter that should be known prior to performing the dual-tip SNOM measurements is the polarization characteristic of the excitation aperture tip. Mode losses due to the fiber bend along the tapered region lead to polarization filtering of the modes propagating inside the fiber. Likewise, a bend in the detection tip results in a polarization-sensitive detection. However, the polarization filtering effect is less pronounced for the multi-mode fiber used for a near-field detection. Since the bend of the fiber determines the polarization of the mode that reaches the exit of the aperture [38], the emission pattern of the excitation tip should be characterized before performing the dual-tip SNOM measurements on the metasurface. We used the dual-tip SNOM setup to characterize the polarization of the emission from the excitation tip aperture. In this regard, we have analyzed

the propagation direction of the SPPs excited on a gold film by the excitation tip. The propagation direction of the excited SPPs corresponds to the polarization of the electric field at the exit of the aperture tip [39, 40]. In the corresponding simulation to reproduce the emission pattern of the aperture tip at air-gold interface, an in-plane magnetic dipole perpendicular to the direction of the electric field polarization was used to model the emission pattern [28, 40]. The same magnetic dipole was used to numerically simulate the emission of the excitation tip on the metasurface.

3 Near-field excitation and detection of the metasurface by the dual-tip SNOM

Before performing the dual-tip SNOM measurements, we used a far-field spectroscopy setup to determine the spectral characteristics of the metasurface. The metasurface consists of silicon nanodisks with a radius of $r = 317$ nm and a height of $h = 237$ nm arranged in square lattice with a lattice constant of $L = 915$ nm on a glass substrate. Figure 2A shows the measured transmittance of the metasurface. The inset of the figure shows the SEM image of the silicon metasurface. For comparison, a simulated spectrum is also included. The numerical simulations were carried out with a commercial FDTD solver, Lumerical.

Although the measurements show a slightly higher transmittance than the simulations, which is due to fabrication imperfections, the metasurface shows very strong dipole resonances. The two minima in Figure 2A correspond to the magnetic dipole (MD) and electric dipole (ED) modes of the metasurface. Figure 2B and C shows the simulated electric and magnetic intensity patterns for one unit cell at the wavelength of the ED mode ($\lambda = 1624$ nm), in the plane $z = 20$ nm above the nanodisk. The excitation source was a plane wave with a y-polarized electric field, which illuminated the metasurface from the far-field. White arrows denote the in-plane polarization vectors of the electric and magnetic fields. We performed the position-dependent near-field measurements of the dielectric metasurface using the dual-tip SNOM. The excitation tip illuminates the metasurface at the ED mode wavelength $\lambda = 1624$ nm. The excitation tip is stationary throughout all measurements. A nanopositioning piezoelectric stage displaced the metasurface relative to the excitation tip. Figures 3A–D and 4A–E are the near-field intensity distributions mapped by the detection tip for the successive displacements of the metasurface along the x- and y-axis, respectively. The initial position of the excitation tip with respect to the metasurface in Figure 3A, $\Delta x = 0$ and Figure 4A, $\Delta y = 0$ was selected arbitrarily. The metasurface displacements Δx and Δy from the initial position are shown on top of each column. The total displacement of the metasurface was about one lattice constant. Due to mechanical and thermal drifts of the excitation tip, we observed an error of ± 0.05 µm for the excitation tip position in each displacement. While it is possible to use smaller displacement steps to cover the displacement of about one lattice constant, we avoided using more steps to prevent the drift of the excitation tip caused by a longer measurement time. For the data normalization in Figures 3A–D and 4A–E each panel was divided by the same value. Once the value was the maximum measured intensities of all panels 3A–D for the metasurface displacements along the x-axis and then for all panels 4A–E for the metasurface displace-

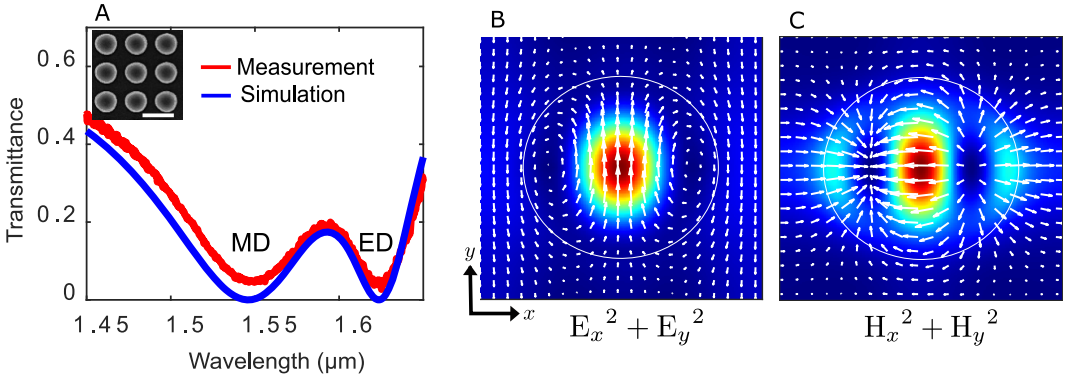

Figure 2: (A) Measured and simulated transmittance for the nanodisk silicon metasurface depicted in the inset with the 1 µm scale bar. Two minima correspond to the wavelengths of the magnetic dipole (MD) and electric dipole (ED) modes of the metasurface. In-plane (B) electric and (C) magnetic field intensity for the ED mode in one unit cell of the metasurface. The white arrows illustrate the polarization vectors of the fields.

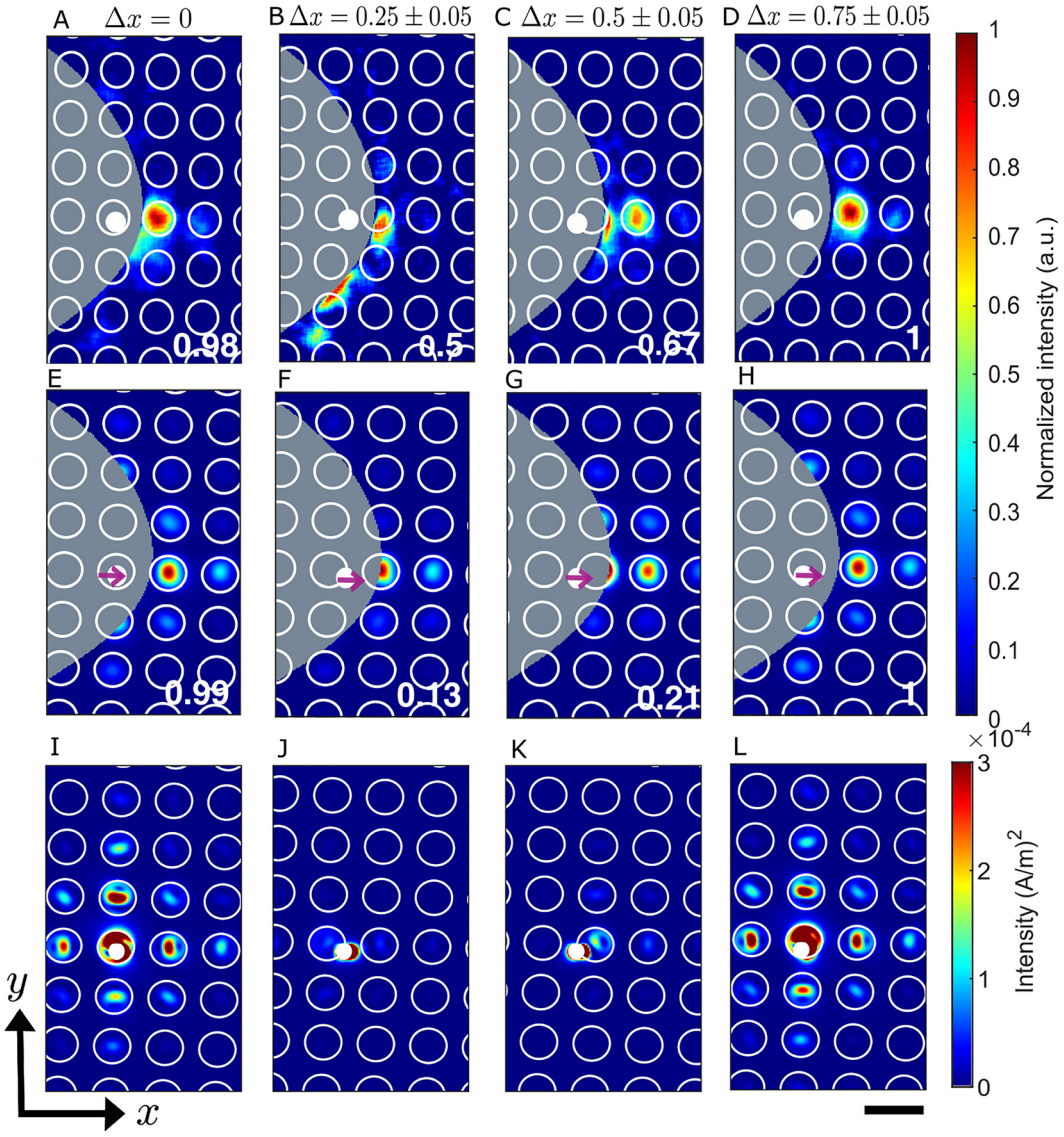

Figure 3: (A)–(D) Measured near-field intensity distributions by the dual-tip SNOM when the metasurface is moved by a displacement of Δx along the x-axis. $\Delta x = 0$ is the initial position. ± 0.05 μm is the respective error due to uncertainty to find the drifts of the excitation tip during the measurements in (B)–(D). White dots indicate the aperture position of the excitation tip in the measurements. For normalizing the data, the measured near-field intensities in (A)–(D) were divided by the maximum measured value of all panels. (E)–(H) Numerical simulations for the in-plane components of the magnetic field intensity for the metasurface displacements in (A)–(D). The gray parabolic-like regions represent the avoidance area. Purple arrows show the position and direction of the magnetic dipole used in the simulations. The simulated intensities with the avoidance area are also normalized, after setting the intensities inside the avoidance area to zero, to the maximum value of the calculated near-field intensity in (E)–(H). Panels (A)–(D) and (E)–(H) share the common color scale while the numbers on the right bottom corners are the maximum normalized intensities in each panel. (I)–(L) Simulation results for the in-plane magnetic field intensities. All the simulation results are shown for the same intensity value to increase the visibility of the near-field intensity patterns. The black scale bar is 1 μm.

ments along the y-axis. In the numerical simulations, the emission from the excitation aperture tip is represented by the in-plane magnetic dipole [41–43]. The white dots with the purple arrows in the middle denote the excitation aperture tip position and the orientation of the magnetic dipole used in the numerical simulations. The magnetic dipole orientation in the simulations was along the x-axis. There is an error of ± 0.1 μm to determine the absolute initial position of the excitation aperture with respect to the metasurface. The gray parabolic-like region is the avoidance area, where no optical signal can be detected in the near-field measurement. White circles mark the edges of the nanodisks. The aperture tip mostly mapped in-plane components of the electromagnetic fields. However, the

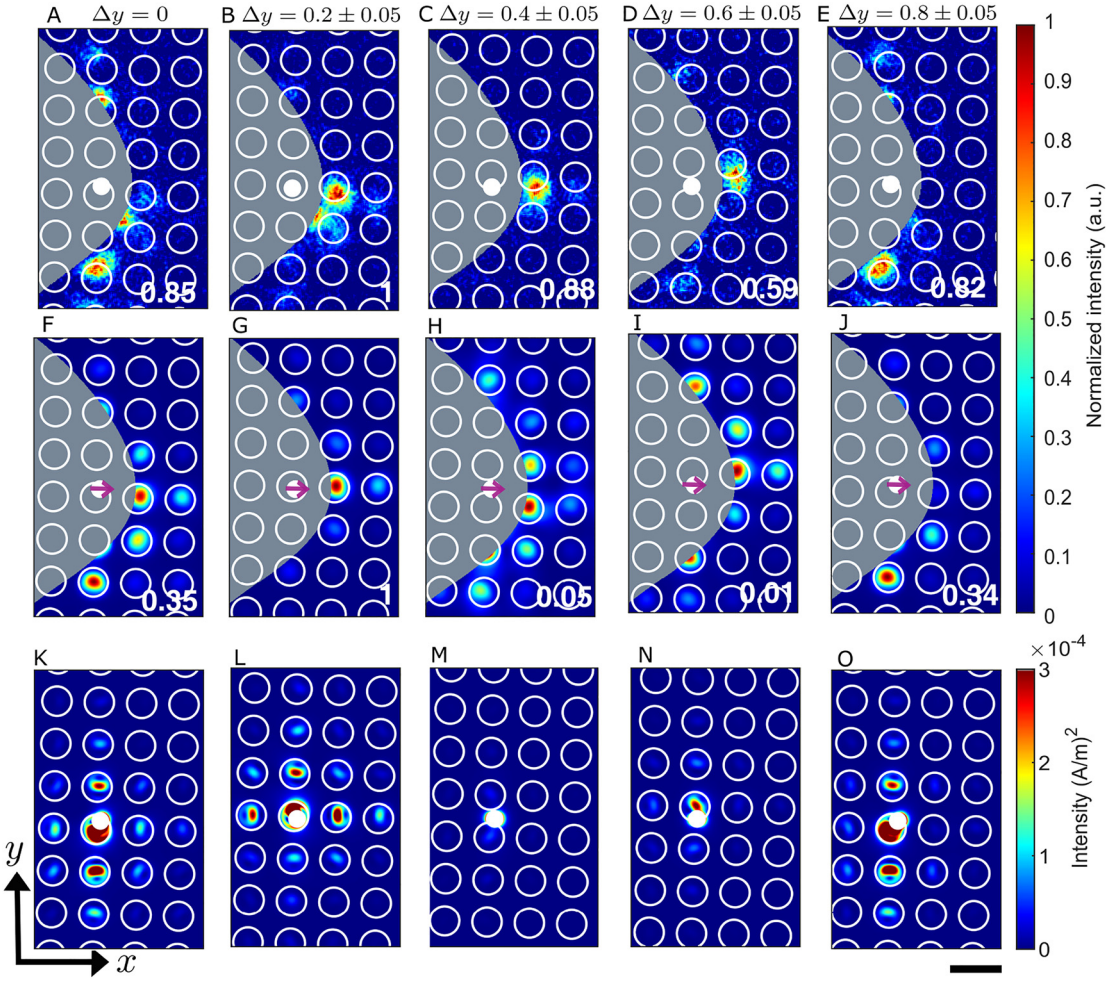

Figure 4: (A)–(E) Measured near-field intensity distributions for the metasurface displacements Δy along y-axis. The initial position is $\Delta y = 0$. White dots indicate the position of the excitation aperture in the measurements. ± 0.05 μm is the error in the displacements (B)–(E) due to the drifts of the excitation tip during the measurements. The measured near-field intensities were divided by the maximum measured value for the normalization. (F)–(J) Numerical simulations of the in-plane magnetic field intensity components for the metasurface displacements in (A)–(E). The gray parabolic-like region is the avoidance area. The purple arrow denotes the magnetic dipole direction and position in the simulations. The simulated intensities, after setting the intensities inside the avoidance areas to zero, were normalized to the maximum calculated near-field intensity. Panels (A)–(E) and (F)–(J) share the common color scale while the numbers on the right bottom corners are the maximum normalized intensities in each panel. (K)–(O) Simulation results (F)–(J) without covering the avoidance area. The simulation results are shown for the same intensity value to increase the visibility of the near-field patterns. The black scale bar is 1 μm.

tilt of the detection tip in the dual-tip SNOM setup, leads to the collection of the electromagnetic components normal to the metasurface plane. These contributions to the collected signal can be considered as negligible due to its smaller magnitude in comparison with the in-plane electromagnetic components near the metasurface. Due to the sensitivity of the detection tip to magnetic fields, only in-plane magnetic field components were considered in the numerical simulations [40, 42, 44]. Figures 3I–L and 4K–O show the simulation results of the magnetic field intensity distributions monitored in a plane 20 nm above the metasurface when it is excited by a magnetic dipole in the same plane. The metasurface was displaced in each simulation with the corresponding retrieved displacements from the experiment. In Figures 3I–L and 4K–O the simulated results are plotted for the same scale to increase the visibility of the details in the near-field intensity distributions. However, the comparison between the measured near-field intensities and the simulation results in Figures 3I–L and 4K–O is not straightforward due to the avoidance area in the measurements where the detection tip cannot map any optical signal. For the sake of comparing the simulations and measurements, in Figures 3I–L and 4K–O, the calculated intensities corresponding to the

avoidance area were set to zero. Figures 3E–H and 4F–J show the simulation results, with the intensities being zero in the avoidance area. For the data normalization after setting the data of the avoidance area to zero in Figures 3E–H and 4F–J, each panel was divided by the same calculated value. Once the value was the maximum calculated intensities of all panels 3E–H for the metasurface displacement along the *x*-axis, and then the maximum calculated intensity of all panels 4F–J for the metasurface displacement along the *y*-axis. The measurements and the calculated intensities with the avoidance area share the same color scale. The numbers on the right bottom corners of each panel denote the maximum intensity in the respective panel.

3.1 *x*-axis displacement of the metasurface

In Figure 3A, the excitation aperture tip is located on top of the nanodisk and a strong near-field intensity is observed on the nanodisk next to the excitation tip position. The corresponding simulated near-field intensity considering the avoidance area in Figure 3E, is in excellent agreement with the experimentally mapped intensity (Figure 3A). However, if we consider Figure 3I, that is the simulation without setting the avoidance area to zero, we can see that the in-plane modes of the metasurface propagate in all directions and their intensities are higher along the *x*- and *y*-axis. Therefore, one could argue that coupling of the excitation tip emission is more efficient along *x*- and *y*-axis and less efficient in diagonal directions. The reason why the mapped near-field intensity in Figure 3A is higher along the *x*-axis is attributed to the asymmetry of the avoidance area. Due to the parabolic shape of the avoidance area, the nearest measurable point from the excitation tip along the *y*-direction is further away than along the *x*-direction. Moreover, since the intensity decays rather quickly from the excitation point, a lower intensity was mapped in the *y*-direction.

As a next step, the excitation tip was placed above the edges of a nanodisk for the displacements in Figure 3B and C. It is observed that the near-field patterns show weaker intensities in Figure 3B and C compared to Figure 3A. The corresponding simulations with the avoidance area in Figure 3F–G also confirm the decrease of the maximum intensities. The slight difference between the pattern of the measured (Figure 3B) and simulated (Figure 3F) near-field intensity distribution is the result of the error in retrieving the exact position of the excitation tip on the metasurface. In Figure 3J and K, we showed the simulations without the avoidance area. The weaker near-field intensities also indicate the lower coupling efficiencies of the excitation tip's emission to the modes of the metasurface.

For the metasurface displacement of about one lattice constant from the initial position, due to the periodicity, the near-field distribution should show the same pattern as the mapped intensity in Figure 3A. This is observed in both measured (Figure 3D) and simulated (Figure 3H) intensities.

3.2 *y*-axis displacement of the metasurface

A displacement of the metasurface along the *y*-axis also leads to different coupling efficiencies and different propagation directions of the in-plane excited modes of the metasurface.

Figure 4A–E exhibit the mapped near-field intensities when the metasurface is displaced along the *y*-axis. In Figure 4A the initial position of the aperture on the upper edge of the nanodisk results in the higher intensity along the *y*-axis. The simulated near-field pattern in Figure 4F shows good agreement with the mapped intensity in Figure 4A. The simulated near-field intensity in Figure 4K also reveals mode propagation mainly along the *y*-axis.

In Figure 4B, the excitation tip is placed almost in the middle of the nanodisk. The mapped intensity is, therefore, higher along the *x*-axis similar to Figure 3A. The numerical result at the respective position in Figure 4G, considering the avoidance area, verifies the measured near-field distribution pattern obtained in the measurement (Figure 4B). The simulation of the near-field intensity without avoidance area (Figure 4L) shows coupling of modes in all directions. As mentioned before, the observation of the higher near-field intensity along the *x*-axis is due to the asymmetry of the avoidance area.

In Figure 4C and D, the excitation tip is positioned on the inner edge of the nanodisk and in between the nanodisks, respectively. The highest intensity is measured along the *x*-axis in both cases. The maximum intensity is lower when the excitation tip is located in between the nanodisks, which indicates a less efficient coupling of the excitation tip's emission to the modes of the metasurface. Therefore, when the excitation tip is on the nanodisk edge or especially in between the nanodisk, the number of available modes that the dipole emission can couple into is lower.

The details of the simulated near-field patterns in Figure 4H and I are not observed in the mapped near-field intensities in Figure 4C and D. The reason is due to the low signal-to-noise ratio of the collected signal by the detection tip. The corresponding simulations without

avoidance area in Figure 4M and N also indicate that the emission from the excitation tip does not couple to the modes of the metasurface efficiently (edge of the nanodisks and in between the nanodisks). Therefore, no details of the near-field distribution are observed in the simulations.

In Figure 4E, the excitation tip is placed nearly at a distance of one period from the initial position of the tip, i.e., in the upper edge of the nanodisk. The mapped near-field pattern shows propagating modes along the *y*-axis. It is observed that the near-field pattern is similar to the intensity distribution obtained for the initial position of the tip (Figure 4A). This corroborates that the displacement along the *y*-axis corresponds to almost one lattice constant. The simulation in Figure 4J shows a good agreement with the measurement result in Figure 4E, which also exhibits modes propagating with a higher intensity along the *y*-axis. Moreover, in Figure 4O, the result of the simulation without avoidance area also shows the higher intensity along the *y*-axis.

Remarkably, the measurement results of the mapped near-field intensities by the dual-tip SNOM are in good agreement with the numerical simulations. The small discrepancies between measurements and simulations can be explained as follows. The slight broadening of the measured near-field intensity patterns, as compared with the simulations, is due to the limited resolution of the detection tip based on its aperture diameter (350 nm). The detection tip cannot resolve features of the near-field intensity that are smaller than its aperture size [26]. As a result, it averages small features in the intensity distributions. Furthermore, due to the asymmetry in the geometries of the excitation and detection tips, the mapped optical and topography signals (white circles on the mapped intensities) experienced different offsets next to the boundary of the avoidance area. (See Supplementary Information).

4 Mapped near-field intensity and partial LDOS

In earlier studies using the single-tip SNOM, the capability of the SNOM to map the partial LDOS was demonstrated theoretically and experimentally [11, 12, 45]. The partial LDOS was mapped using the particular configuration of the illumination SNOM (forbidden light SNOM) [46]. In the forbidden light SNOM, propagating components of the electromagnetic fields were filtered, and the evanescent waves were converted into traveling waves and detected in the far-field below the sample, similar to the leakage radiation microscopy [47]. Thus, the details of the mapped partial LDOS were determined by the amount of evanescent waves that reached the far-field. In contrast to the forbidden light SNOM, the detection tip of the dual-tip SNOM can directly map the evanescent waves above the metasurface. The integrated mapped near-field intensity in the plane of detection using the dual-tip SNOM is also expected to be proportional to the partial LDOS at the location of the excitation tip's aperture, similar to the intensity measured using the forbidden light SNOM [12]. Therefore, mapped near-field intensities by the dual-tip SNOM at different excitation points could always be used to compare the partial LDOS at corresponding positions on the nanostructures. More importantly, the mapped near-field intensity provides valuable information concerning the correlation between the excitation and detection points (CDOS). Hence, verifying the relationship between the integrated near-field intensity and the partial LDOS would also allow the measurement of the CDOS in disordered and complex photonic systems by the dual-tip SNOM [21, 48].

In the dual-tip SNOM measurements, the dipole-like emission from the excitation aperture tip corresponds to the emission of a magnetic dipole oriented along the $x-$direction. Therefore, the magnetic partial LDOS is the relevant quantity in our measurement. The magnetic partial LDOS quantifies the number and strength of the excited modes at a certain position based on the strength and polarization vectors of the magnetic field projected along the magnetic dipole direction [10]. According to Figure 2C, visualizing the magnetic field intensity of the ED mode and the in-plane polarization vectors, the maximum contribution to the partial LDOS from the ED mode is obtained for a magnetic dipole polarized along the *x*-axis and placed at the position where the magnetic field has maximum intensity. Although the partial LDOS takes into account the contribution of all available modes, and not only a single mode, at the ED resonance wavelength of ($\lambda = 1624$ nm), modes are dominated by the ED contribution as it can be observed from the multipolar decomposition of the scattering cross-section for a single nanodisk of the metasurface (see Figure S3 in the Supplementary Information). The behavior of the mapped near-field intensity distributions by the dual-tip SNOM can be explained with the same argument. Since the polarization of the dipole-like emission from the excitation tip is fixed during the measurement, the partial LDOS is different for various positions of the excitation tip relative to the metasurface. The change of the partial LDOS is reflected in the distinct near-field intensity patterns around the excitation tip. However, from different near-field patterns, it cannot be concluded that the LDOS is modified. The modification of the partial LDOS

would result from the change of the integrated near-field intensities (powers) over the scan window.

The partial LDOS is indeed related to the power radiated by a dipole [26]. In other words, the power radiated by the dipole emitter is proportional to the partial LDOS. In this regard, we have calculated the normalized power and compare it with the integrated measured near-field intensities. Since both normalized radiated power and integrated near-field intensity should be proportional to the partial LDOS, we expect that they follow the same behavior.

Figure 5A shows the normalized integrated intensity calculated from the mapped intensity patterns in Figure 3A–D (measurement) and Figure 3E–H (simulation) for the metasurface displacements along the x-axis. The intensity values are integrated over the scan window, excluding the avoidance area. Likewise, Figure 5C exhibits the normalized integrated mapped near-field intensities in Figure 4A–E (measurement) and Figure 4F–J (simulation) for the metasurface displacements along the y-axis. In Figure 5A and C, raw data of the measured integrated near-field intensities, after subtracting the constant value due to the measurement noise, were scaled to the maximum value of the integrated intensities in the simulations. In Figure 5A and C, the horizontal error bars for the measured data indicate the error in determining the displacement of the metasurface along the x- and y-axis due to the excitation tip's drift during the measurements. This error could be one reason for the observed difference between the integrated near-field intensities of the measured and calculated data. Moreover, the influence of the two tips when they are laterally close within the region of shear forces could be another reason for the observed discrepancy in the measured near-field intensity comparing with simulation. It is important to note that the integrated near-field intensity can only determine the partial LDOS qualitatively. In other words, when the near-field intensity is mapped for different positions of the excitation tip relative to the nanostructures using the dual-tip SNOM, the partial LDOS at the respective position is one of the quantities that can be calculated.

Figure 5B and D shows the normalized radiated power P_{rad}/P_0 and power loss P_{loss}/P_0 for the metasurface displacements Δx and Δy where P_0 is the power radiation of a dipole on a glass substrate without silicon nanodisks. We simulated the radiative and non-radiative power emitted from a magnetic dipole, located at $z = 20$ nm above the metasurface, for the displacement values in the measurements. In general, the dipole emission is coupled to radiative and non-radiative modes. However, the losses

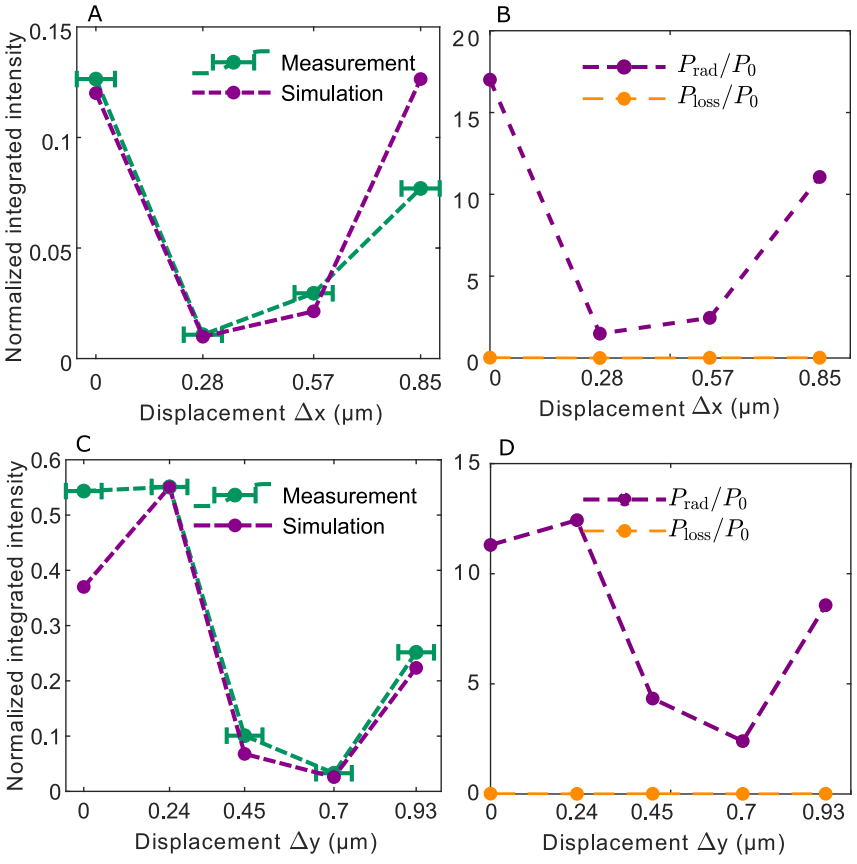

Figure 5: (A) Normalized integrated intensities for the measurements in Figure 3A–D and simulations in Figure 3D–H for Δx displacements. The error bar only shows the error in finding displacements due to the drift of the excitation tip during the measurements. (B) Corresponding normalized radiative power and the power loss of the magnetic dipole. (C) Normalized integrated intensities for the measurements in Figure 4A–E and simulations in Figure 4H–J for Δy displacements. (D) Corresponding normalized radiative power and the power loss of the magnetic dipole for the same Δy displacements. The integrated intensities were calculated for the raw data of simulations and measurements. To normalize the integrated intensity of the measurements, they were scaled to the maximum value of the integrated intensity in the simulations.

are negligible in the analyzed spectral range of the silicon metasurface; thus, all the emission corresponds to the radiative power.

Changes in the integrated mapped near-field intensity in Figure 5A and C follow the same trend as changes of the normalized power in Figure 5B and D, respectively. We can conclude that the integrated near-field intensity, even excluding the avoidance area, still indicates how the normalized power and, consequently, the partial LDOS changes. In addition, we calculated the integrated near-field intensity and the power radiation for smaller increments of the metasurface displacements than those performed in the experiment (see Figure S3 Supplementary Information). These simulations were performed to obtain more points in Figure 5 and corroborated that the integrated near-field intensity, excluding the avoidance area, follows the same behavior as the normalized radiation power. As a result, the dual-tip SNOM would indeed predict the behavior of partial LDOS at a certain position of the quantum emitter relative to the photonic nanostructures.

5 Conclusions

Using a dual-tip SNOM, we have shown the measurement of the near-field intensity distribution due to the dipole emission at different positions on a silicon metasurface. The mapped near-field intensities demonstrated that the direction and extent of the excited modes highly depend on the position and the orientation of the dipole emission relative to the nanostructures. More strikingly, we could show that the integrated mapped near-field intensity is proportional to the partial local density of states (LDOS) at the excitation position. Hence, the automated dual-tip SNOM can be a promising technique to measure the cross-density of states (CDOS). Moreover, the aperture tip could be replaced with the quantum emitter on the uncoated tip apex to investigate the near-field interaction of the quantum emitter with the photonic system. Although all principles that work for a single SNOM operating in illumination or detection mode are also applicable for the dual-tip SNOM [26, 30], extra challenges particular to the automated dual-tip SNOM should be addressed to enable the dyadic Green's function measurement. In this regard, the perturbation of the near-field distribution due to the presence of two aperture tips and their influence on the image formation when two tips are laterally close should be investigated with rigorous numerical calculations. Despite all experimental challenges, the automated dual-tip SNOM technique is a step closer to mapping the dyadic near-field Green's function and the quantities associated with it [49–51]. Thus, point source excitation and detection in the near-field, accessible by the dual-tip SNOM, can establish a novel approach to study unknown aspects of light–matter interaction in complex photonic systems.

Acknowledgment: We gratefully acknowledge S. Saravi for the fruitful discussions. N. A. and A. B. acknowledge financial support from the German Academic Exchange Service (DAAD) and Alexander von Humboldt Foundation, respectively.

Author contribution: All the authors have accepted responsibility for the entire content of this submitted manuscript and approved submission.

Research funding: This work has been funded by the Deutsche Forschungsgemeinschaft (DFG – German Research Foundation) through the international research training group (Project-ID 259607349-GRK2101), the priority program SPP 1839 Tailored Disorder (Project number 278747906), and Collaboration Research Center NOA (Project-ID 39881677-SFB 1375), as well as by the European Union: project METAFAST-899673-FETOPEN-H2020.

Conflict of interest statement: The authors declare no conflicts of interest regarding this article.

References

[1] S. Slussarenko and G. J. Pryde, "Photonic quantum information processing: a concise review," *Appl. Phys. Rev.*, vol. 6, no. 4, 2019, Art no. 041303.

[2] A. Blais, S. M. Girvin, and W. D. Oliver, "Quantum information processing and quantum optics with circuit quantum electrodynamics," *Nat. Phys.*, vol. 16, no. 3, pp. 247–256, 2020.

[3] C. L. Degen, F. Reinhard, and P. Cappellaro, "Quantum sensing," *Rev. Mod. Phys.*, vol. 89, no. 3, 2017, Art no. 035002.

[4] S. Pirandola, B. R. Bardhan, T. Gehring, C. Weedbrook, and S. Lloyd, "Advances in photonic quantum sensing," *Nat. Photonics*, vol. 12, no. 12, pp. 724–733, 2018.

[5] T. Gefen, A. Rotem, and A. Retzker, "Overcoming resolution limits with quantum sensing," *Nat. Commun.*, vol. 10, no. 1, pp. 1–9, 2019.

[6] F. Laux, N. Bonod, and D. Gérard, "Single emitter fluorescence enhancement with surface lattice resonances," *J. Phys. Chem. C*, vol. 121, no. 24, pp. 13280–13289, 2017.

[7] V. Flauraud, R. Regmi, P. M. Winkler, et al., "In-plane plasmonic antenna arrays with surface nanogaps for giant fluorescence enhancement," *Nano Lett.*, vol. 17, no. 3, pp. 1703–1710, 2017.

[8] R. M. Bakker, D. Permyakov, Y. F. Yu, et al., "Magnetic and electric hotspots with silicon nanodimers," *Nano Lett.*, vol. 15, no. 3, pp. 2137–2142, 2015.

[9] R. Regmi, J. Berthelot, P. M. Winkler, et al., "All-dielectric silicon nanogap antennas to enhance the fluorescence of single molecules," *Nano Lett.*, vol. 16, no. 8, pp. 5143–5151, 2016.
[10] W. L. Barnes, S. A. Horsley, and W. L. Vos, "Classical antennas, quantum emitters, and densities of optical states," *J. Opt.*, vol. 22, no. 7, 2020, Art no. 073501.
[11] G. C. des Francs, C. Girard, J. C. Weeber, et al., "Optical analogy to electronic quantum corrals," *Phys. Rev. Lett.*, vol. 86, no. 21, p. 4950, 2001.
[12] C. Chicanne, T. David, R. Quidant, et al., "Imaging the local density of states of optical corrals," *Phys. Rev. Lett.*, vol. 88, no. 9, 2002, Art no. 097402.
[13] N. Caselli, F. Intonti, F. La China, et al., "Generalized fano lineshapes reveal exceptional points in photonic molecules," *Nat. Commun.*, vol. 9, no. 1, pp. 1–8, 2018.
[14] N. Caselli, F. Riboli, F. La China, et al., "Tailoring the photon hopping by nearest-neighbor and next-nearest-neighbor interaction in photonic arrays," *ACS Photonics*, vol. 2, no. 5, pp. 565–571, 2015.
[15] K. Cognée, W. Yan, F. La China, et al., "Mapping complex mode volumes with cavity perturbation theory," *Optica*, vol. 6, no. 3, pp. 269–273, 2019.
[16] N. Caselli, T. Wu, G. Arregui, et al., "Near-field imaging of magnetic complex mode volume," *ACS Photonics*, vol. 8, no. 5, pp. 1258–1263, 2021.
[17] E. Castanié, V. Krachmalnicoff, A. Cazé, R. Pierrat, Y. De Wilde, and R. Carminati, "Distance dependence of the local density of states in the near field of a disordered plasmonic film," *Opt. Lett.*, vol. 37, no. 14, pp. 3006–3008, 2012.
[18] F. Riboli, N. Caselli, S. Vignolini, et al., "Engineering of light confinement in strongly scattering disordered media," *Nat. Mater.*, vol. 13, no. 7, pp. 720–725, 2014.
[19] N. Caselli, F. Intonti, F. La China, et al., "Near-field speckle imaging of light localization in disordered photonic systems," *Appl. Phys. Lett.*, vol. 110, no. 8, 2017, Art no. 081102.
[20] D. S. Wiersma, "Disordered photonics," *Nat. Photonics*, vol. 7, no. 3, pp. 188–196, 2013.
[21] K. Vynck, R. Pierrat, R. Carminati, et al., *Light in Correlated Disordered Media*, 2021, arXiv preprint arXiv:2106.13892.
[22] V. Parigi, E. Perros, G. Binard, et al., "Near-field to far-field characterization of speckle patterns generated by disordered nanomaterials," *Opt. Express*, vol. 24, no. 7, pp. 7019–7027, 2016.
[23] A. Cazé, R. Pierrat, and R. Carminati, "Spatial coherence in complex photonic and plasmonic systems," *Phys. Rev. Lett.*, vol. 110, no. 6, 2013, Art no. 063903.
[24] R. Carminati, A. Cazé, D. Cao, et al., "Electromagnetic density of states in complex plasmonic systems," *Surf. Sci. Rep.*, vol. 70, no. 1, pp. 1–41, 2015.
[25] A. Dogariu and R. Carminati, "Electromagnetic field correlations in three-dimensional speckles," *Phys. Rep.*, vol. 559, pp. 1–29, 2015.
[26] L. Novotny and B. Hecht, *Principles of Nano-Optics*, Cambridge, Cambridge University Press, 2012.
[27] K. Rustomji, M. Dubois, P. Jomin, et al., "Complete electromagnetic dyadic green function characterization in a complex environment—resonant dipole-dipole interaction and cooperative effects," *Phys. Rev. X*, vol. 11, no. 2, 2021, Art no. 021004.
[28] N. Abbasirad, J. Berzins, K. Kollin, et al., "A fully automated dual-tip scanning near-field optical microscope for localized optical excitation and detection in the visible and near-infrared," *Rev. Sci. Instrum.*, vol. 90, no. 5, 2019, Art no. 053705.
[29] B. Le Feber, J. E. Sipe, M. Wulf, L. Kuipers, and N. Rotenberg, "A full vectorial mapping of nanophotonic light fields," *Light Sci. Appl.*, vol. 8, no. 1, pp. 1–7, 2019.
[30] N. Rotenberg and L. Kuipers, "Mapping nanoscale light fields," *Nat. Photonics*, vol. 8, no. 12, pp. 919–926, 2014.
[31] J. S. Clausen, E. Højlund-Nielsen, A. B. Christiansen, et al., "Plasmonic metasurfaces for coloration of plastic consumer products," *Nano Lett.*, vol. 14, no. 8, pp. 4499–4504, 2014.
[32] S. Dobmann, A. Kriesch, D. Ploss, and U. Peschel, "Near-field analysis of bright and dark modes on plasmonic metasurfaces showing extraordinary suppressed transmission," *Adv. Opt. Mater.*, vol. 2, no. 10, pp. 990–999, 2014.
[33] A. E. Klein, N. Janunts, S. Schmidt, et al., "Dual-snom investigations of multimode interference in plasmonic strip waveguides," *Nanoscale*, vol. 9, no. 20, pp. 6695–6702, 2017.
[34] Y. Masaki, K. Tomita, Y. Kojima, and F. Kannari, "Measurement of propagation of ultrafast surface plasmon polariton pulses using dual-probe scanning near-field optical microscopy," *Appl. Opt.*, vol. 58, no. 21, pp. 5595–5601, 2019.
[35] I. Staude, T. Pertsch, and Y. S. Kivshar, "All-dielectric resonant meta-optics lightens up," *ACS Photonics*, vol. 6, no. 4, pp. 802–814, 2019.
[36] A. S. Solntsev, G. S. Agarwal, and Y. Y. Kivshar, "Metasurfaces for quantum photonics," *Nat. Photonics*, vol. 15, no. 5, pp. 327–336, 2021.
[37] B. Le Feber, N. Rotenberg, and L. Kuipers, "Nanophotonic control of circular dipole emission," *Nat. Commun.*, vol. 6, no. 1, pp. 1–6, 2015.
[38] D. Ploss, A. Kriesch, H. Pfeifer, P. Banzer, and U. Peschel, "Generation and subwavelength focusing of longitudinal magnetic fields in a metallized fiber tip," *Opt. Express*, vol. 22, no. 11, pp. 13744–13754, 2014.
[39] B. Hecht, H. Bielefeldt, L. Novotny, Y. Inouye, and D. Pohl, "Local excitation, scattering, and interference of surface plasmons," *Phys. Rev. Lett.*, vol. 77, no. 9, p. 1889, 1996.
[40] A. E. Klein, N. Janunts, M. Steinert, A. Tunnermann, and T. Pertsch, "Polarization-resolved near-field mapping of plasmonic aperture emission by a dual-snom system," *Nano Lett.*, vol. 14, no. 9, pp. 5010–5015, 2014.
[41] E. Devaux, A. Dereux, E. Bourillot, et al., "Local detection of the optical magnetic field in the near zone of dielectric samples," *Phys. Rev. B*, vol. 62, no. 15, p. 10504, 2000.
[42] H. W. Kihm, J. Kim, S. Koo, et al., "Optical magnetic field mapping using a subwavelength aperture," *Opt. Express*, vol. 21, no. 5, pp. 5625–5633, 2013.
[43] S. Schmidt, A. Klein, T. Paul, et al., "Image formation properties and inverse imaging problem in aperture based scanning near field optical microscopy," *Opt. Express*, vol. 24, no. 4, pp. 4128–4142, 2016.
[44] S. Vignolini, F. Intonti, F. Riboli, et al., "Magnetic imaging in photonic crystal microcavities," *Phys. Rev. Lett.*, vol. 105, no. 12, p. 123902, 2010.
[45] C. Girard, "Near fields in nanostructures," *Rep. Prog. Phys.*, vol. 68, no. 8, p. 1883, 2005.

[46] B. Hecht, D. W. Pohl, H. Heinzelmann, and L. Novotny, ""tunnel" near-field optical microscopy: Tnom-2," in *Photons and Local Probes*, Dordrecht, Springer, 1995, pp. 93–107.
[47] A. Drezet, A. Hohenau, D. Koller, et al., "Leakage radiation microscopy of surface plasmon polaritons," *Mater. Sci. Eng. B*, vol. 149, no. 3, pp. 220–229, 2008.
[48] R. Carminati and M. Gurioli, *Purcell Effect with Extended Sources: The Role of the Cross Density of States*, 2021, arXiv preprint arXiv:2107.13980.
[49] V. Krachmalnicoff, D. Cao, A. Cazé, et al., "Towards a full characterization of a plasmonic nanostructure with a fluorescent near-field probe," *Opt. Express*, vol. 21, no. 9, pp. 11536–11545, 2013.
[50] D. Cao, A. Cazé, M. Calabrese, et al., "Mapping the radiative and the apparent nonradiative local density of states in the near field of a metallic nanoantenna," *ACS Photonics*, vol. 2, no. 2, pp. 189–193, 2015.
[51] D. Bouchet, M. Mivelle, J. Proust, et al., "Enhancement and inhibition of spontaneous photon emission by resonant silicon nanoantennas," *Phys. Rev. Appl.*, vol. 6, no. 6, 2016, Art no. 064016.

Supplementary Material: The online version of this article offers supplementary material (https://doi.org/10.1515/nanoph-2021-0429).